High performance motion control of the METIS Cold Chopper Mechanism

Huisman, Robert; Paalvast, S.; Brandl, B.; van den Dool, T.C.; Eggens, Marchienus; Janssen, H.; Aitink-Kroes, G.; Molster, F.; Teuwen, M.; Venema, L.

Published in:
IEEE/ASME Transactions on Mechatronics

DOI:
10.1109/TMECH.2016.2578678

Publication date:
2016

High-Performance Motion Control of the METIS Cold Chopper Mechanism

Robert Huisman, Sander Paalvast, Bernhard R. Brandl, Teun van den Dool, Martin Eggens, Huub Janssen, Gabby Aitink-Kroes, Frank Molster, Maurice Teuwen, Lars Venema, and Bayu Jayawardhana, *Senior Member, IEEE*

***Abstract*—We present the main results of the performance test campaign of the Mid-Infrared European Extremely Large Telescope Imager and Spectrograph (METIS) Cold Chopper Demonstrator (MCCD). This tip/tilt mirror, which operates at a temperature of 77 K, is one of the critical components in the METIS for the European Extremely Large Telescope. The performance requirements of the MCCD relate to the field of fast and very accurate reference tracking. We discuss the applicability of different high-performance motion control strategies and describe the control synthesis of a repetitive and of a novel hybrid controller. We identified the presence of nonlinearities in the plant, which limits the performance of the hybrid controller. The repetitive controller shows very promising results and can handle the nonlinearities in the system. This experimental phase concludes the MCCD program, which was initiated to verify the feasibility of a high-performance cryogenic tip/tilt mirror at an early stage in the METIS development. Because of the very promising test results, no significant changes to the hardware will be implemented. We believe that minor adjustments will suffice to meet all requirements of the final hardware after integration with the METIS instrument.**

***Index Terms*—Control synthesis, high-performance motion control, hybrid control, hysteresis, repetitive control, tip/tilt mechanism.**

Manuscript received July 19, 2015; revised November 13, 2015 and March 08, 2016; accepted April 16, 2016. Date of publication June 08, 2016; date of current version October 13, 2016. Recommended by Technical Editor X. Chen.

R. Huisman and M. Eggens are with SRON—The Netherlands Institute for Space Research, 9700 AV Groningen, The Netherlands (e-mail: r.huisman@sron.nl; m.eggens@sron.nl).

S. Paalvast, H. Janssen, and M. Teuwen are with Janssen Precision Engineering, 6199 AG Maastricht-Airport, The Netherlands (e-mail: sander.paalvast@jpe.nl; huub.janssen@jpe.nl; maurice.teuwen@jpe.nl).

B. Brandl is with Leiden Observatory, Leiden University, 2300 RA Leiden, The Netherlands, and also with the Faculty of Aerospace Engineering, Delft University of Technology, 2629 HS Delft, The Netherlands (e-mail: brandl@strw.leidenuniv.nl).

T. C. van den Dool is with TNO Optomechatronics, 2628 CK Delft, The Netherlands (e-mail: teun.vandendool@tno.nl).

G. Aitink-Kroes is with the Optical/Infrared Instrumentation Group, NOVA, 7991 PD Dwingeloo, The Netherlands (e-mail: kroes@astron.nl).

F. Molster is with the Leidse Instrumentmakers School, 2333CC Leiden, The Netherlands, and also with NOVA, 2333 CA Leiden, The Netherlands (e-mail: molster@lis.nl).

L. Venema is with ASTRON, 7990 AA Dwingeloo, The Netherlands.

B. Jayawardhana is with the Faculty of Mathematics and Natural Sciences, University of Groningen, 9747 AG Groningen, The Netherlands (e-mail: b.jayawardhana@rug.nl).

Color versions of one or more of the figures in this paper are available online at http://ieeexplore.ieee.org.

Digital Object Identifier 10.1109/TMECH.2016.2578678

I. Introduction

THE MID-INFRARED European Extremely Large Telescope Imager and Spectrograph Cold Chopper (MCC) mechanism is one of the critical components in the Mid-Infrared European Extremely Large Telescope Imager and Spectrograph (METIS) [1] for the European Extremely Large Telescope (E-ELT) [2]. With its 39-m dish, the E-ELT will be the largest optical/infrared telescope ever. The E-ELT will see first light in 2024 and is being developed by the European Southern Observatory.

METIS will be one of the first three scientific instruments on the E-ELT, covering the thermal infrared wavelength range. At these wavelengths, very accurate subtraction of the spatially and temporally varying background is essential. This is usually done by beam chopping, i.e., alternating the optical beam between science target and a reference location on the nearby sky at a frequency of a few Hertz. While the beam chopping is traditionally done by the telescope's secondary mirror, this option does not exist for the E-ELT and an alternative solution within METIS had to be found.

This work is part of the MCC demonstrator (MCCD) project, which was initiated to show the feasibility of a high-performance chopping mirror inside a cryogenic instrument at an early stage in the METIS development. The MCC is a tip/tilt mirror at the pupil position of METIS. Tilting the MCC in two dimensions moves the orientation of the telescope beam on the sky without having to move the telescope.

Different chopping and scanning strategies can be considered [3]. The focus here is on the so-called chopping or beam switching technique, where the mirror quickly chops between two or more exactly reproducible mirror positions. From differential measurements, the sky background and detector noise can be derived and subtracted from the image which contains the source.

Several challenging performance requirements drive the design of both hardware and control of the MCC (see Table VII). Most notably are the requirements for short-beam switching times (i.e., high observing efficiency with small overheads, which requires short settling times) and very accurate positional repeatability (which is required for sharp images in coadded long-term exposures). Meeting these requirements simultaneously is very challenging from a control perspective, which is related to the field of high-performance motion control.

Different control strategies are available for high-performance motion control of nanopositioning mechanisms. What these techniques generally have in common is the

application of a feedforward (FF) signal for fast stepping, typically but not necessarily in parallel with a feedback controller for noise reduction and robustness. Although the design of this FF signal is usually based on the available knowledge of the plant dynamics (model based approach), the details about the generation of the FF signal [4], [5] and the shaping of the reference profile [6], [7] can vary a lot.

When reference profiles of a repetitive nature are applied, as for this application, one can also consider the use of a repetitive controller [8], [9]. Different from the model-based approach, the repetitive loop generates the FF signal by learning with every repetition.

We developed a hybrid control strategy [10], [11], which applies an FF input in open loop during the step, to avoid possible negative effects of the closed-loop controller because of its limited bandwidth w.r.t. the frequency content of the reference profile as discussed in [10] and [12], and switches to closed loop during the observation periods. The method involves resetting, memorizing, and switching between different sets of control states at fixed moments during an observation. Resetting of the control states is similar to reset control [13] and impulsive control [14], where the state of a feedback controller is subject to sudden changes dictated by the reference profile or the tracking error. A clear distinction with our method, however, is the definition of the initial control states at the start of every observation period and that we perform the step in open loop.

We compare the experimental results applying this strategy with that of a repetitive controller and discuss the different issues related to both methods.

In Section II, we describe in detail the system identification of the hardware, which revealed the presence of hysteresis in the system. The applied control strategies are described in Section III and the experimental results are given in Section IV, where we also discuss some of the issues regarding the implementation of the control strategy. Finally, the conclusions of the test campaign are given in Section V.

II. System Identification

A. Hardware and Test Setup

For details about the MCCD mechatronic design, the reader is referred to [15]. Here, we summarize the key mechatronic elements of the mechanism and describe the experimental test setup. Details about the dynamical behavior of the system are given in Section II-B.

A schematic overview of the MCCD mechanism, which is designed to operate in cryogenic conditions, is shown in Fig. 1. It has three degrees of freedom (DoF), which composes of rotation around the x- and y-axis (tip/tilt) and translation along the z-axis. The triangular support structure with the circular mirror body is supported by three monolithic struts with elastic hinges to constrain the three undesired DoFs without introducing backlash or friction. Displacements are measured by three Attocube position sensors (type: FPS3010) based on the principle of laser interferometry and actuation is provided by three voice coil actuators. These voice coil actuators were especially developed for the MCCD. In the design, the back iron is detached from

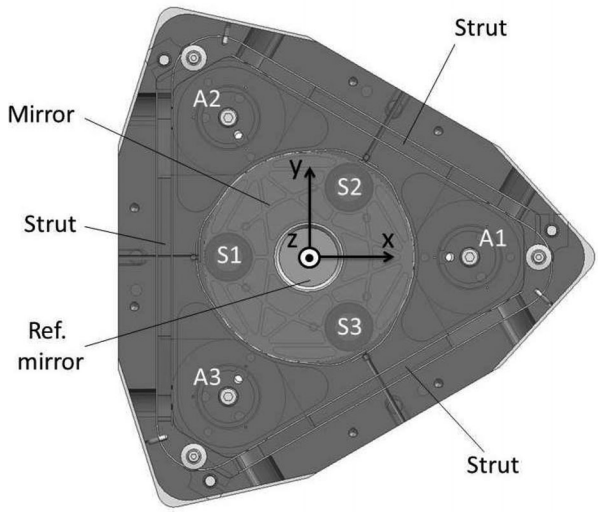

Fig. 1. Schematic overview of the MCCD mechanism. Triangular support structure with circular mirror body is made transparent to show the location of the sensors (S1, S2, and S3) and actuators (A1, A2, and A3). The fixed reference mirror at the heart of the structure is used for test purposes only and will not be part of the final MCC. The coordinate system is also indicated. Design by Janssen Precision Engineering (JPE).

the permanent magnet. It is fixed to the base structure, which limits the amount of moving mass (magnet only) of the actuator and, therefore, considerably reduces the moment of inertia of the mirror body.

The mechanism dynamics (inertia, spring constant, and damping) are designed to be rotationally symmetric. The multiple-input multiple-output system is converted to three decoupled single-input single-output systems by applying the following matrix transformations:

$$\begin{bmatrix} z \\ \theta_x \\ \theta_y \end{bmatrix} = \begin{bmatrix} \frac{1}{3} & \frac{1}{3} & \frac{1}{3} \\ 0 & \frac{1}{\sqrt{3}r_s} & -\frac{1}{\sqrt{3}r_s} \\ \frac{2}{3r_s} & -\frac{1}{3r_s} & -\frac{1}{3r_s} \end{bmatrix} \begin{bmatrix} z_1 \\ z_2 \\ z_3 \end{bmatrix} \tag{1}$$

$$\begin{bmatrix} F_1 \\ F_2 \\ F_3 \end{bmatrix} = \begin{bmatrix} \frac{1}{3} & 0 & \frac{-2}{3r_f} \\ \frac{1}{3} & \frac{1}{\sqrt{3}r_f} & \frac{1}{3r_f} \\ \frac{1}{3} & \frac{-1}{\sqrt{3}r_f} & \frac{1}{3r_f} \end{bmatrix} \begin{bmatrix} F_z \\ M_{\theta_x} \\ M_{\theta_y} \end{bmatrix}. \tag{2}$$

Equation (1) relates the three sensor readouts (z_1, z_2, and z_3) to the three DoFs of the system, where r_s is the radial distance of the sensors to the heart of the mirror. Equation (2) converts the control inputs (F_z, M_{θ_x}, and M_{θ_y}) for the different DoFs to the individual force inputs (F_1, F_2, and F_3) of the actuators. Here, r_f is the radial distance of the actuators to the heart of the mirror.

The experimental setup is sketched in Fig. 2. Tests are performed in a cryostat at an operating temperature of 77 K. The sensor electronics are placed outside the cryostat. The optical measurement signal is guided to the MCCD hardware by three

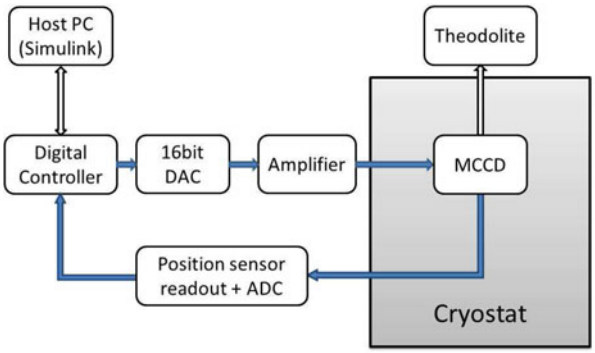

Fig. 2. Block diagram showing the general building blocks of the experimental setup. The MCCD is placed in a cryostat and tests are performed at an operating temperature of 77 K.

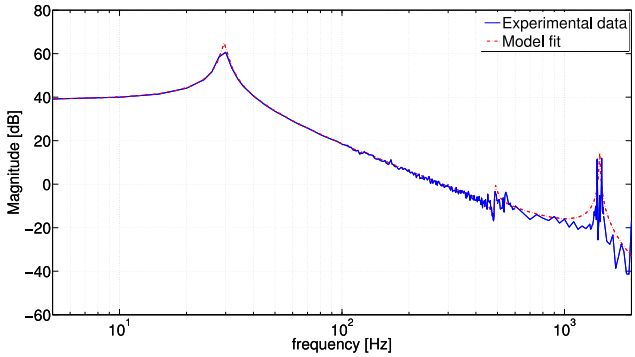

Fig. 3. Bode magnitude plot of θ_x. Experimental data and fitted eighth-order model. Experimental data based on sinesweep (Freq. range 5–600 Hz and 1400–1500 Hz covered with 5-Hz frequency resolution. Other regime covered with 50 Hz res.)

glass fibers. Calibration of the 2-DoF rotational motion is performed using a theodolite. The MATLAB xPC target platform is used to implement the digital controller (designed in MATLAB Simulink using a host PC) on a target machine. The system runs at a sampling rate of 10 kHz.

B. Plant Dynamics

System identification is performed by the method of frequency analysis. The experimental data are generated applying a high-resolution sinesweep over the frequency regime from 5 Hz to 2 kHz and fitting the steady-state response of the system (input and output) to a sine profile. This provides us with the phase shift and gain information required to generate the bode plot. We only use the magnitude plot for model fitting because of the limited accuracy of the phase information.

Fig. 3 shows the bode magnitude plot of the open-loop plant for θ_x. The dominant resonance frequencies of the mechanism are clearly visible. Table I gives these dominant resonance frequencies and compares them to the results from a detailed finite-element analysis (FEA) [16].

The resonant behavior at approximately 500 Hz cannot be explained by the mechanism dynamics. The same is true for a small, but relevant resonance at 125 Hz. These resonances do not

TABLE I
DOMINANT RESONANCES OF MCCD FOR θ_x ORIENTATION; EXPERIMENTAL AND FEA RESULTS GENERATED USING CREO SIMULATE AND CREO PARAMETRIC SOFTWARE

Measured	FEA
29.6 Hz	29.0 Hz
1405.0 Hz	1443.1 Hz
1470.0 Hz	1491.0 Hz

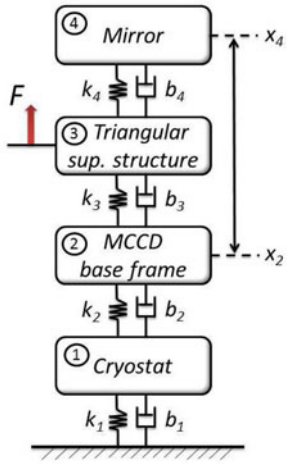

Fig. 4. Noncollocated lumped mass system representative for the dominant eighth-order θ_x-dynamics. The actuator force is applied at the triangular support structure and displacements are measured at the mirror surface relative to the MCCD base frame.

show up in the FEA and, despite the rotational symmetry of the MCCD, are not present in the θ_y dynamics. They are believed to originate from the test setup, e.g., the cryostat, whose structural dynamics are not symmetrical w.r.t. the introduced forces as a result of θ_x or θ_y rotation.

Due to the influence of the cryostat, we consider a noncollocated lumped mass system as shown in Fig. 4 to describe the θ_x-dynamics. This results in an eighth-order system with five stable zeros, i.e., two complex conjugated pairs close to, respectively, the 125- and the 500-Hz resonance and one zero at high frequency. Based on this system, we model the θ_x-dynamics including the dominant resonance at 29.6 Hz, a skew notch at 125 and 487 Hz, and a broad resonance at 1440 Hz (to account for the two sharp resonances between 1.4 and 1.5 kHz). The high-frequency zero has very limited influence on the system response and we choose to ignore this in our system model.

The θ_y-dynamics are modeled as a fourth-order plant excluding the two resonances related to the cryostat. Finally, the z-dynamics are less critical and can be approximated by a second-order plant.

Using the transfer function given by

$$P(s) = \frac{a_n s^n + a_{n-1} s^{n-1} + \cdots + a_1 s + a_0}{b_n s^n + b_{n-1} s^{n-1} + \cdots + b_1 s + b_0} \tag{3}$$

where $a_n, ..., a_0, b_n, ..., b_0$ are coefficients to be fitted; the final system models for the different DoFs are given in Table II.

TABLE II
LAPLACE TRANSFORM COEFFICIENTS FOR ALL THREE DOFS

	P_{θ_x}	P_{θ_y}	P_z
a_0	2.77×10^{27}	2.53×10^{14}	1.01×10^{4}
a_1	1.00×10^{23}	-	-
a_2	4.95×10^{21}	-	-
a_3	3.72×10^{16}	-	-
a_4	5.11×10^{14}	-	-
b_0	3.09×10^{25}	2.76×10^{12}	1.59×10^{4}
b_1	9.71×10^{21}	7.77×10^{8}	10.48
b_2	9.51×10^{20}	8.19×10^{7}	1
b_3	4.85×10^{16}	77.80	-
b_4	1.60×10^{15}	1	-
b_5	1.45×10^{10}	-	-
b_6	1.68×10^{8}	-	-
b_7	178.5	-	-
b_8	1	-	-

The given coefficients are related to the standard transfer function given in (3). These are rounded values taken from the 64-bit floating point numbers provided by MATLAB.

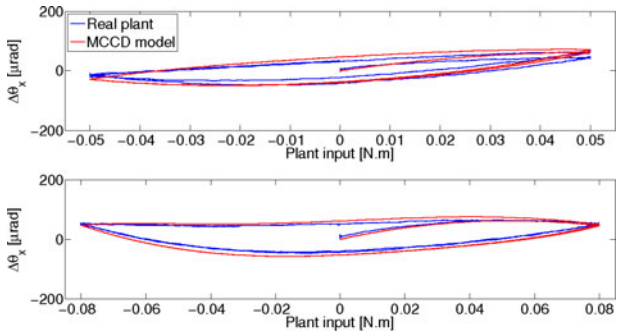

Fig. 5. Observed hysteresis in θ_x and fitted model for sine inputs spanning different parts of the chop range (0.05-N·m input corresponds to 4.5-mrad output, 0.08 N·m corresponds to 7.2 mrad). Max. displacement (at 0 input) caused by hysteresis is approximately 0.7% of rotated angle. NB: Linear term of system response is taken out to clearly expose the hysteresis.

Comparison of the simulated step response with experimental data shows a good match for the 1-mrad chop range for which the identification has been performed [see, for example, Fig. 7 (0° offset result)].

A detailed system model, including the weak resonance at 125 Hz, is required for an accurate FF design. This is discussed in more detail in Section III-A.

C. Nonlinear Behavior

The experimental results revealed the presence of nonnegligible nonlinearities in the system. This is shown in Fig. 5, where the linear component of the system response is taken out to clearly expose a slightly deformed hysteresis curve. The hysteresis is caused by the relative displacement of the constant magnetic field, generated by the permanent magnet, with respect to the back iron in the actuators. As a result, the magnetic field strength, at any point in the back iron, depends on the orientation of the chopper, and the back iron material exhibits its magnetic hysteresis curve when the mirror is rotated.

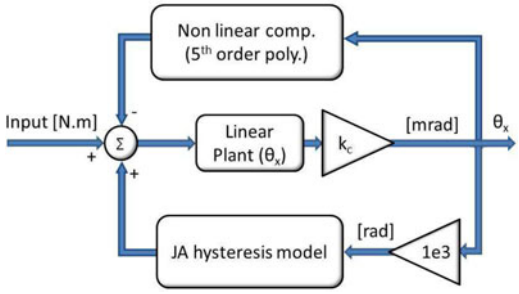

Fig. 6. Nonlinear MCCD plant model, including a JA model to represent the hysteresis behavior in the system and an extra nonlinear term to account for the observed deformation of the hysteresis curve.

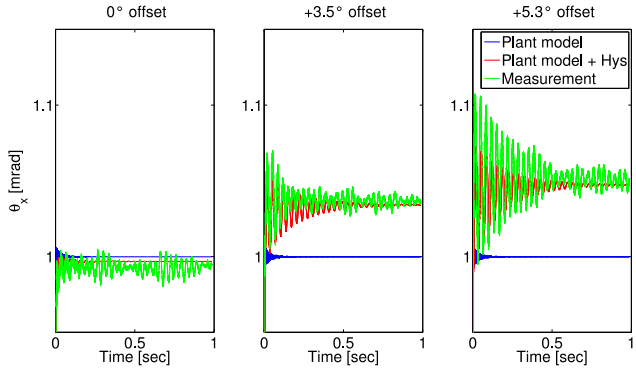

Fig. 7. Effect of hysteresis on FF response (open loop). Comparison between experiment, linear model, and model with hysteresis. Close up at end position for: Left: 0 to +1 mrad step Middle: 3.5 to 4.5 mrad step and Right: 5.3 to 6.3 mrad step. NB: Start position is set to zero in all plots for easy comparison.

The slight deformation of the hysteresis curve is caused by the position-dependent reluctance in the magnetic circuit. The reluctance is maximal in the center position $(\theta = 0)$ and reduces with increasing angle. This introduces negative magnetic stiffness. As the reluctance of the magnetic circuit is inversely proportional to the magnetic field strength, it also makes the force constant of the actuator position dependent.

In Section III-A, we describe the hybrid control method. It includes the design of a feedback controller and of an FF signal. The nonlinearity has only a small effect on the response of the system, and it is not necessary to consider this in the design of the feedback controller. On the other hand, the design of the FF signal is based on a model of the plant. It largely determines the settling time of the mechanism, and its performance is directly related to the accuracy of the system model.

In an effort to account for the nonlinearity in the FF signal design, we included a Jiles–Atherton (JA) hysteresis model [17] in the system description. The JA model is based on physical laws describing the magnetization process in ferromagnetic materials and is thought to be appropriate for the current application. In parallel, we added a nonlinear component in the form of a fifth-order polynomial to account for the deformation of the hysteresis curve. Fig. 6 shows the basic building blocks of the nonlinear MCCD model. Both operators use the angular

TABLE III
TUNED PARAMETERS OF NONLINEAR MCCD MODEL

JA parameters	tuned values	Poly. coef.	tuned values
α	1×10^{-3}	p_1	7.289990×10^{-9}
a	0.44	p_2	2.101289×10^{-9}
k	1750.70	p_3	-2.663815×10^{-6}
c	0.22	p_4	8.192315×10^{-6}
M_s	0.44	p_5	1.059444×10^{-4}
k_c	0.99	p_6	1.608167×10^{-3}

NB: The k_c parameter is not part of the JA model

orientation of the mechanism as input parameter and affect the input ([N·m]) to the linear plant model.

It is known that tuning the JA model parameters is a difficult process, which is strongly dependent on the choice of initial conditions and often results in nonideal solutions [18]. As we have to include six extra parameters in our model to also account for the nonlinearity, related to the position-dependent force constant of the system, tuning of the complete set of parameters becomes even more challenging. We tuned the parameters by hand, after which we used MATLAB's nonlinear curve-fitting procedure (lsqcurvefit) for fine tuning. This, however, did not result in further optimization of the parameters.

The tuned model parameters are given in Table III. The model response is included in Fig. 5. The fit shows the same characteristic response to a sine input for different amplitudes. The accuracy of the model is, however, limited. This is supported by the experimental results given in Fig. 7, showing the response of the system to an FF input applied at different offset positions in the chop range. The FF input was generated on the basis of the linear model and designed to deliver a 1-mrad step. The response of the linear model (blue line) is independent of the offset position in the chop regime, while the experimental result clearly shows the dependence on start position, which indicates that hysteresis phenomena have taken place. This hypothesis is corroborated by the simulation result when we include the hysteresis model.

The nonlinear plant model provides valuable insight in the nonlinear behavior of the MCCD hardware and fully explains all observed effects. However, from a control design perspective, as the model complexity drastically increases when the hysteresis model (with its 12 parameters) is included, and as the accuracy of the modeled response is limited, we decided not to use the nonlinear model for the FF design.

III. CONTROL SYNTHESIS

A. Hybrid Controller

In this paper, we will implement a hybrid controller based on [10] and [11]. As the proposed strategy requires switching of the system between FF and feedback control, which involves resetting, memorizing, and switching between different sets of control states at every start of a scanning period, proof of output regulation is not trivial. The structure of the controller and the results on hybrid output regulation [19] motivated us to formulate the complete system in the hybrid framework.

Let us recall some main results from [10] and [11], where an internal model principle is used to solve a chopping scanning control problem based on hybrid system theory. A hybrid system is a system which exhibits both continuous-time and discrete-time dynamics denoted, respectively, as flow and jump dynamics. We utilize the hybrid formalism and notation as given in [20].

1) Hybrid System Formulation and Control Design Criteria: For compactness of presentation, we consider below the formulation for the 1-DoF dynamics. Extension to higher dimensions is, however, trivial as the MCCD is rotationally symmetric and the θ_x and θ_y dynamics are decoupled.

The plant dynamics of the MCCD can compactly be formulated as

$$\left.\begin{aligned} \dot{x} &= A_G x + B_G u, \quad x(t_0) = x_0 \quad \forall (x,u) \in \mathbb{R}^n \times \mathbb{R} \\ y &= C_G x \end{aligned}\right\} \tag{4}$$

where A_G, B_G, and C_G are the state-space matrices, which realize the transfer function in (3). The input u represents the current input signal to the actuator and the output y is the measured angular displacement.

We define the control input u by

$$u(t) = \begin{cases} u_j(t) & \forall t \in [(j+1)t_{\text{obs}} + jt_s, (j+1)(t_{\text{obs}} + t_s)] \\ & \forall j \in \mathbb{N} \\ v(t), & \text{otherwise} \end{cases} \tag{5}$$

where t_{obs} defines the length of the observation period between two consecutive steps and t_s is the step time. v is an additional control signal that can be used for feedback control.

Observe that by applying u_j to (4) for any arbitrary initial state x_j and initial time t_j, we have

$$x(t_j^+) = M_G x(t_j) + N_j \tag{6}$$

where the plant transition matrix $M_G := \exp(A_G t_s)$ and

$$N_j = \int_{t_j}^{t_j^+} \exp(A_G(t_j^+ - \lambda)) B_G u_j(\lambda) d\lambda.$$

Equation (6) resembles the jump dynamics in the hybrid system framework.

Now, by first defining the hybrid time domain E as follows:

$$E := \bigcup_{j=\mathbb{N}} [jt_{\text{obs}}, (j+1)t_{\text{obs}}] \times \{j\}$$

the dynamics of x on E can equivalently be described by the following hybrid system:

$$\left.\begin{aligned} \dot{\tau}_c &= 1 \\ \dot{\zeta} &= A_G \zeta + B_G v, \quad \zeta(0,0) = \zeta_0 \\ & \quad \forall (\tau_c, \zeta, v) \in [0, t_{\text{obs}}] \times \mathbb{R}^n \times \mathbb{R} \\ \tau_c^+ &= 0 \\ \zeta^+ &= M_G \zeta + N_j \quad \forall (\tau_c, \zeta) \in t_{\text{obs}} \times \mathbb{R}^n \\ y &= C_G \zeta \end{aligned}\right\} \tag{7}$$

where $\zeta_0 = x(0)$, v is the additional control signal applied during the flow periods, and τ_c is a clock variable with a dwell time t_{obs}, which defines the moment of jumping of the system.

This reformulation of the plant dynamics into hybrid setting opens the possibility of assigning optimal control solutions during the first t_s seconds (which are computed offline for the nominal positions) and implementing a hybrid feedback controller to stabilize the system.

Following the hybrid output regulation setting as in [19], we can adopt the following exosystem which generates the reference signal r and is also defined on the hybrid time domain E as above:

$$\left.\begin{aligned} \dot{\tau}_c &= 1 \\ \dot{w} &= Sw, \quad w(0,0) = w_0 \quad \forall (\tau_c, w) \in \mathcal{W} \\ \tau_c^+ &= 0 \\ w^+ &= Jw \quad \forall (\tau_c, w) \in \mathcal{W} \cap (\{t_{\text{obs}}\} \times \mathbb{R}^s) \\ r &= Qw \end{aligned}\right\} \tag{8}$$

with

$$S = \begin{bmatrix} \Upsilon & 0 \\ 0 & 0 \end{bmatrix}_{(4q \times 4q)} \quad \Upsilon = \begin{bmatrix} 0 & \omega_n & 0 & 0 \\ -\omega_n & 0 & 0 & 0 \\ 0 & 0 & 0 & 1 \\ 0 & 0 & 0 & 0 \end{bmatrix}$$

$$J = \begin{bmatrix} 0 & I_{(4*(q-1))} \\ M_e^{-1} & 0 \end{bmatrix} \quad M_e = \exp(\Upsilon * t_{\text{obs}})$$

$$Q = \begin{bmatrix} 1 & 0 & 1 & 0 & 0_{(1\times(4(q-1)))} \end{bmatrix}$$
$$w = \begin{bmatrix} w_1 & w_2 & \dots & w_q \end{bmatrix}$$
$$w_p = \begin{bmatrix} w_{p1} & w_{p2} & w_{p3} & w_{p4} \end{bmatrix}.$$

Finally, $\mathcal{W} := \{(\tau_c, w) \colon \tau_c \in [0, t_{\text{obs}}], w \in W(\tau_c)\}$, where the set valued mapping $\tau_c \to W(\tau_c) \subset \mathbb{R}^s$ is continuous with compact values. The parameter $q \in \mathbb{N}$ defines the number of integration periods that constitute a single repetition of the reference profile. $p \in \{1, 2, \dots, q\}$ and ω_n is the angular velocity of the oscillator. The matrix M_e is the transition matrix related to Υ. The presence of the inverse of this term in the jump matrix J guarantees that the active exostate variables are reset to their initial value after every period of flow, even if $t_{\text{obs}} \neq 2\pi/\omega_n$.

The exosystem can generate all astronomical observation modes that are discussed in [3], except for spiral chopping, by choosing the appropriate initial conditions $w_0 := w(0,0)$ in combination with the required form of N_j to jump between the different flow sets.

We remark that for the current application we only consider square wave chopping which greatly simplifies the exosystem description. We present the full description here to illustrate the necessity to reset the control states at the end of each flow period. For square wave chopping ($q = 2$), the matrices can be reduced to the following form:

$$S = \begin{bmatrix} 0 & 0 \\ 0 & 0 \end{bmatrix} \quad J = \begin{bmatrix} 0 & 1 \\ 1 & 0 \end{bmatrix} \quad Q = \begin{bmatrix} 1 & 0 \end{bmatrix}. \tag{9}$$

Based on this exosystem description and applying the internal model principle as in [19], the hybrid controller can now be described in the following way:

$$\left.\begin{aligned} \dot{\tau}_c &= 1 \\ \dot{\xi} &= A_C \xi + B_C e, \quad \xi(0,0) = \xi_0 \\ &\quad \forall (\tau_c, \xi, e) \in [0, t_{\text{obs}}] \times \mathbb{R}^m \times \mathbb{R} \\ \tau_c^+ &= 0 \\ \xi^+ &= \Phi \xi + \Psi e \\ &\quad \forall (\tau_c, \xi, e) \in \{t_{\text{obs}}\} \times \mathbb{R}^m \times \mathbb{R} \\ v &= C_C \xi + D_C e \end{aligned}\right\} \tag{10}$$

where

$$A_C = \begin{bmatrix} \star & 0 \\ 0 & S \end{bmatrix}$$
$$B_C = \begin{bmatrix} \star & k_1 & 0 & k_2 & k_3 & 0_{(1\times(4(q-1)))} \end{bmatrix}^T$$
$$C_C = \begin{bmatrix} \star & Q \end{bmatrix} \qquad D_C = \begin{bmatrix} \star \end{bmatrix}$$
$$\Phi = \begin{bmatrix} I_\star & 0 \\ 0 & J \end{bmatrix} \quad \Psi = \begin{bmatrix} \star \\ 0 \end{bmatrix}$$

the parameters k_1, k_2, and k_3 are controller gains. The elements in $\star$ are related to the design of a robust feedback controller and can be designed according to each different application. The identity matrices in Φ indicate that the states related to $\star$ are not changing as a result of the jump. The J in the ϕ matrix is identical to the jump matrix of the exosystem. Again the inverse of M_e guarantees that in the steady state, the active control states related to the internal model jump back to the correct initial state at the end of the flow period. The variable e is the error signal, i.e., $e = r - C_G \zeta$. Again, this general form can be reduced to the special case of square wave chopping by applying (9) and reformulating the input matrix as $B_C = \begin{bmatrix} \star & k_1 & 0 \end{bmatrix}^T$.

Finally, the complete closed-loop hybrid system is given by

$$\left.\begin{aligned} \dot{\tau}_c &= 1, \quad \dot{w} = Sw, \quad w(0,0) = w_0 \\ \begin{bmatrix} \dot{\zeta} \\ \dot{\xi} \end{bmatrix} &= \mathcal{H}_{cl} \begin{bmatrix} \zeta \\ \xi \end{bmatrix} + \mathcal{L}_{cl} w, \quad \begin{bmatrix} \zeta(0,0) \\ \xi(0,0) \end{bmatrix} = \begin{bmatrix} \zeta_0 \\ \xi_0 \end{bmatrix} \\ &\quad \forall ((\tau_c, w), \zeta, \xi) \in \mathcal{W} \times \mathbb{R}^n \times \mathbb{R}^m \\ \tau_c^+ &= 0, \quad w^+ = Jw \\ \begin{bmatrix} \zeta^+ \\ \xi^+ \end{bmatrix} &= \mathcal{J}_{cl} \begin{bmatrix} \zeta \\ \xi \end{bmatrix} + \mathcal{M}_{cl} w \\ &\quad \forall ((\tau_c, w), \zeta, \xi) \\ &\quad \in (\mathcal{W} \cap (\{t_{\text{obs}}\} \times \mathbb{R}^s)) \times \mathbb{R}^n \times \mathbb{R}^m \end{aligned}\right\} \tag{11}$$

with

$$\mathcal{H}_{cl} := \begin{bmatrix} A_G - B_G D_C C_G & B_G C_C \\ -B_C C_G & A_C \end{bmatrix} \quad \mathcal{L}_{cl} := \begin{bmatrix} B_G D_C Q \\ B_C Q \end{bmatrix}$$
$$\mathcal{J}_{cl} := \begin{bmatrix} M_G & 0 \\ -\Psi C_G & \Phi \end{bmatrix} \quad \mathcal{M}_{cl} := \begin{bmatrix} N_{w_j} \\ \Psi Q \end{bmatrix}$$

where N_j is related to the exostate through N_{w_j}, i.e., $N_j := N_{w_j} w$.

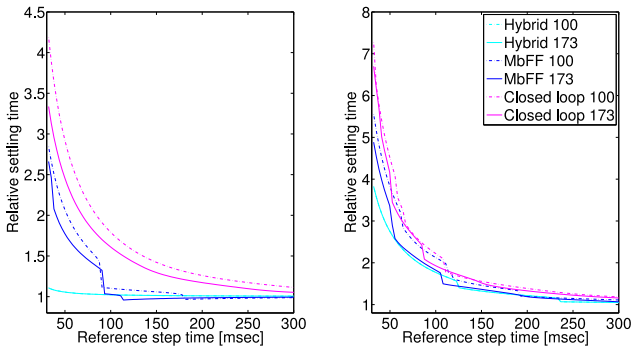

Fig. 8. Effect of step time of reference profile on settling time of system configurations given in Table IV for the hybrid, MbFF, and closed-loop only control strategies (Left: results for conf. 1 and 2. Right: results for conf. 3 and 4). The relative settling is defined as the settling time of the plant normalized by the applied reference step time. The Hybrid 100 and 173 results largely overlap because of the limited influence of the PID controller after the step (as a result of the very small error signal).

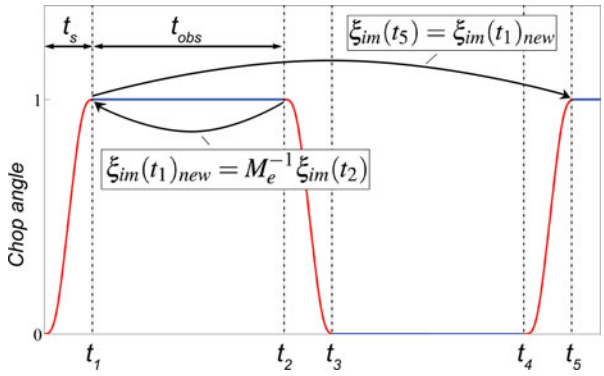

Fig. 9. Chopping timeline related to hybrid controller (first repetition only). The step (red curve) is performed applying FF only (u_j). During the observation periods (blue curve) the hybrid controller is active (v). The reset and memory actions are visualized by the arrows. The control states related to the internal model (ξ_{im}) are reset at time t_2 to the corresponding values at t_1. These states are applied as initial condition during the next repetition at the same observation position. (The same applies to the second observation position). We remark that for square wave chopping the internal model consists of a simple integrator and resetting of the control states is actually not required ($M_e{}^{-1} = I$). The reset action in the figure illustrates the more general case when richer exosystem dynamics (described by Υ) are considered.

Based on this reformulation of the plant dynamics in the hybrid system framework, we can define the chopper scanning control problem as follows.

2) Chopper Scanning Hybrid Control Problem: Design a hybrid controller (10) for the hybrid plant (7) such that the closed-loop system (11) has bounded trajectories and $\lim_{t+j\to\infty} e(t,j) = 0$ uniformly.

The following result gives necessary and sufficient conditions to solve the chopper scanning hybrid control problem. This can be used for synthesis of the hybrid controller with the considered plant dynamics.

Let ϕ_{cl} be the state transition matrix of the flow dynamics

$$\begin{bmatrix} \dot{\zeta} \\ \dot{\xi} \end{bmatrix} = \mathcal{H}_{cl} \begin{bmatrix} \zeta \\ \xi \end{bmatrix}.$$

In other words, $\phi_{cl}(t_{\rm obs}) = \exp(\mathcal{H}_{cl} t_{\rm obs})$ and $\phi_{cl}(t_0) = I_{n+m}$.

Proposition III.1 Assume that the restriction of $\mathcal{H}_{cl}$ to the active subspace is Hurwitz. Then, there exists an attractive invariant manifold $\mathcal{M}$ such that $Qw - C_G\zeta = 0$ if and only if

$$\gamma := \left| \sigma_{\max} \left(\prod_{h=0}^{l-1} \mathcal{J}_{cl_{(l-h)}} \phi_{cl}(t_{obs_{(l-h)}}) \right) \right| < 1 \qquad (12)$$

where $\sigma_{\max}$ is the largest eigenvalue of the matrix and l is the number of scans contained in the smallest repeating sequence of scans with different $t_{\rm obs}$. In particular, we have that $e = r - C_G\zeta \to 0$ as $t + j \to \infty$.

If we satisfy condition (10), the plant asymptotically converges to the invariant manifold which satisfies zero error tracking (this also implies a bumpless transition when switching between FF and feedback control). For the proof of Proposition 3.1, the reader is referred to [10] and [11].

A typical timeline for square wave chopping, applying the hybrid control strategy, is given in Fig. 9. Indicated are the periods where FF or feedback control is applied. The arrows visualize the reset and memory actions.

3) Simulation Results for Stepping Applying MbFF and Hybrid Control: To illustrate why we perform the step in open loop, we simulated the effect of the step time of the reference profile on the settling time of a second order plant for the model based feed forward (MbFF) and the hybrid strategy. For completeness, we also included the result when applying the feedback loop without the FF path. The FF signal is based on an inverse plant model which exhibits frequency-dependent inaccuracies. We applied a proportional integral derivative (PID) controller which was tuned for a certain bandwidth and limited overshoot of the closed-loop plant. The different configurations studied are summarized in Table IV. For clarity, the effect of noise and disturbances is excluded from the results as, for the field of nanopositioning, this will typically affect the positional

TABLE IV
PLANT CONFIGURATIONS STUDIED TO ILLUSTRATE THE EFFECT OF REFERENCE STEP TIME ON SETTLING

	Plant	Inverse plant model	PID parameters	Cl. bw. [rad/s]
1	$\frac{10^4}{s^2+2\times10^2 s+10^4}$	$\frac{10^2 s^2+2\times10^4 s+10^6}{s^2+2\times10^3 s+10^6}$	$k_p=2$, $k_i=102$, $k_d=9.83\times10^{-3}$	100
2			$k_p=3.47$, $k_i=173$, $k_d=1.73\times10^{-2}$	173
3	$\frac{10^4}{s^2+10^2 s+10^4}$	$\frac{10^6 s^2+1.2\times10^8 s+10^{10}}{s^2+2\times10^5 s+10^{10}}$	$k_p=1.12$, $k_i=81.5$, $k_d=3.85\times10^{-3}$	100
4			$k_p=2.57$, $k_i=137$, $k_d=1.21\times10^{-2}$	173

Configurations 1 and 2 represent a critically damped plant. The FF signal is based on a plant model inverse with high-frequency inaccuracies modeled by a 1000 rad/s bw. low-pass filter. Configurations 3 and 4 describe a plant with a resonance. The model mismatch is in the limited representation of the resonance. For both scenarios, PID controllers are tuned with different cl. bandwidths.

TABLE V
INFLUENCE OF PLANT RESONANCES ON SETTLING WHEN APPLYING A FF SIGNAL BASED ON THE SECOND-ORDER PLANT MODEL FOR A STEP FROM $\theta_x = 0$ TO 8.5 MRAD

Plant model	Overshoot [μrad]	Settling [ms]
Second-order (30 Hz)	0	4.9
Fourth-order (30 Hz + 125 Hz)	29	320
Fourth-order (30 Hz + 500 Hz)	11	72
Fourth-order (30 Hz + 1500 Hz)	23	80
Complete eight-order	61	320

The resonances considered in the different plant models are given in the table. NB: The complete eight-order plant also settles within 4.9 ms when applying an FF signal based on the eight-order plant model.

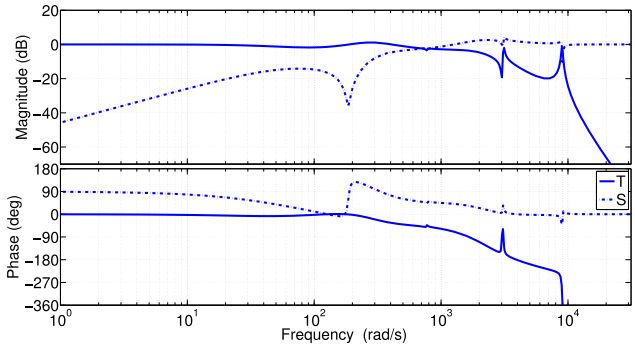

Fig. 10. Bode plot of complementary sensitivity (T) and sensitivity function (S) of the closed-loop plant for θ_x.

stability of the plant before it has a significant effect on settling time. Plant constraints are not considered in the simulation.

Fig. 8 shows the results of the simulations. The hybrid controller outperforms the MbFF for fast reference profiles. For slower reference profiles, the closed loop improves the tracking of the reference and the MbFF approach shows slightly better results. As can be expected, increasing the closed-loop bandwidth reduces the settling time.

The results vary with every specific configuration, but, generally speaking, it can be concluded that for fast reference profiles, with respect to the typically limited controller bandwidth, open-loop stepping performs better.

4) Design of FF Input u_j as Defined in (5): The FF signal is generated by applying quadratic programming to the following optimization problem with input constraints:

$$\min_{u_j \in U} \| x_d(t_s) - x(t_s) \|_2 \tag{13}$$

where U is the set of allowed control inputs $U := \{u_j \in \mathbb{R}^n : |u_{j\,i}| \leq 4.2\text{N.m}\}$, $x_d(t_s)$ is the desired plant state at the end of the step (at time t_s) and $x(t_s)$ is the realized end state as a result of the discrete FF input sequence. This approach can handle input constraints and deals with the discrete nature of the FF input naturally.

We recognize that, because of the high-frequency reference signal in relation to the typically limited bandwidth of the closed-loop controller, fast settling can only be achieved by accurate FF design and not by error convergence after switching to closed loop. Therefore, we use the full 5-ms settling time specification for our FF signal. This maximizes the number of individual discrete steps of the FF which allows for better norm reduction of (13), and it reduces the maximum forces exerted on the mechanism. The effect of which is the reduction of resonant behavior after the step as a result of model uncertainties and nonmodeled dynamics. Furthermore, as this also limits the peak currents generated by the amplifier, this gives the possibility to reduce the amplifier output range. As reduction of the amplifier range typically means reduction of the amplifier noise levels, this has a direct positive effect on the positional stability of the mechanism.

Table V summarizes the result of a simulation where we applied an accurately designed FF signal based on the second-order MCCD plant model (including only the 29.6-Hz rigid body mode) to different model plant configurations. This clearly shows the necessity to include the higher order resonances in the FF-design.

5) Feedback controller: The feedback controller for θ_x has been tuned by loop shaping. It consists of a skew notch filter to compensate the large phase shift introduced by the dominant resonance at 29.6 Hz, an integrator, required for constant reference tracking and a first-order low-pass filter for high-frequency cutoff. The complete controller, discretized by the Tustin method, is then given by

$$C_{\theta_x} = \frac{0.1722z^4 - 0.3337z^3 - 0.01048z^2 + 0.3337z - 0.1617}{z^4 - 3.311z^3 + 4.085z^2 - 2.228z + 0.4531}.$$

In Fig. 10, the bode plots of both the sensitivity function $S = (1 + PC)^{-1}$ and the complementary sensitivity function $T = PC(1 + PC)^{-1}$ of the closed-loop plant are given. T shows good tracking ability at low frequencies. S was tuned for sufficient amplifier noise and disturbance attenuation below 100 Hz. The slight peaking of the Bode magnitude plot of S above 200 Hz (max. of 4 dB at 500 Hz) is allowed because of the low sensor noise in the system. The gain and phase margins of the closed-loop system are, respectively, 14.3 dB and 82°, from which we can conclude that the feedback loop is robustly stable. The value of γ, as defined in (12), is 0.36, so we satisfy the necessary and sufficient condition for output regulation of the hybrid controller.

Because of the symmetry in the system, and because we do not specifically shape the 125- and 487-Hz resonances, the same controller can be applied to the θ_y DoF. For the control of the z-displacement, it suffices to apply a discrete PID controller with $k_p = 89$, $k_i = 1000$, and $k_d = 0.56$ with a 4012.6 filter bandwidth (forward Euler discretization method).

B. Repetitive Controller

Fig. 11 shows the repetitive control layout. The repetitive loop is placed in parallel with the feedback controller described in Section III-A. The repetitive loop consists of a so-called L-filter for phase compensation, a Q-filter to add robustness, and an internal model which can generate any repetitive signal with period N.

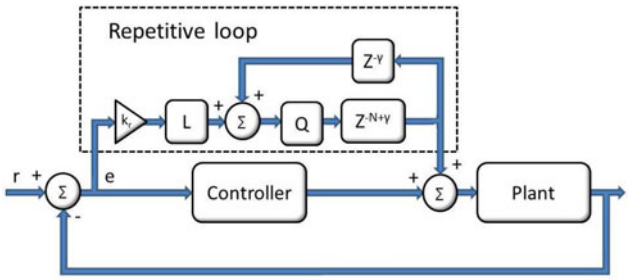

Fig. 11. Repetitive control layout. The repetitive loop is placed in parallel with the standard feedback controller. N is the number of discrete samples in one repetition.

The learning update law of the repetitive loop can be formulated as follows:

$$z^N U_r(z) = Q(z)(U_r(z) + z^\gamma L(z) k_r E(z)) \tag{14}$$

where $z^N U_r(z)$ is the new input which will be applied during the next repetition and is constructed from the input of the current repetition $U_r(z)$ and from the error $z^\gamma E(z)$ as a result of this input. From the feedback loop, we have

$$E(z) = -S_p(z) U_r(z) \tag{15}$$

where $S_p = P/(1+PC)$ is the plant sensitivity function. Combining (14) and (15) gives

$$z^N E(z) = Q(z)(1 - z^\gamma S_p(z) k_r L(z)) E(z)$$

which can be interpreted as the error propagation with every repetition, from which, it can directly be concluded that the error converges monotonically if $|Q(1 - z^\gamma S_p k_r L)| < 1$ for all frequencies up to the Nyquist frequency. Taking $L = {S_p}^{-1}, k_r = 1$, and $\gamma = 0$ theoretically delivers perfect tracking after only one iteration (dead-beat solution). However, an exact inverse is typically not realizable as the inverse of S_p often is nonproper or even unstable as a result of, respectively, a proper or nonminimum phase S_p. Different techniques, such as ZPETC [21], are available for the design of L, but the match is typically not exact and plant uncertainties and nonmodeled dynamics further limit the accuracy of the filter design. The lead term z^γ can be used to partly compensate for the phase lag introduced by the nonideal L-filter as described in [9]. The Q-filter can be designed as a low-pass filter to allow for monotonic error convergence, but this comes at the cost of reduced tracking performance.

The reproducibility is generally considered to be a measure for the tracking accuracy that can be attained by repetitive control. The reproducibility of the MCCD for chopping is $\Delta\theta < 10\,\mu$rad during the step and $\Delta\theta < 2\,\mu$rad during the integration periods.

In our experiment, as we are interested to explore the maximum settling performance using the repetitive method, we take $Q = 1$. This allows for maximum error reduction at the cost of monotonic convergence. We avoided inversion of S_p but used an inverse of the fourth-order θ_y-dynamics of the plant as our L-filter, where we added a fourth-order Butterworth filter to make the transfer function proper. We are aware that sampling of a continuous-time system may lead to the introduction of RHP zeros in the discrete model [22], which in turn can cause problems during system inversion. To avoid this problem, we designed the filter in continuous time, after which the L-filter was discretized by the Tustin method. The resulting filter is then given by

$$L = \frac{0.048z^4 + 6.253e-5z^3 - 0.096z^2 - 2.939e-5z + 0.048}{z^4 - 3.187z^3 + 3.876z^2 - 2.124z + 0.441}.$$

To avoid interference between the feedback controller and the repetitive loop, we only close the loop after convergence of the repetitive controller.

Because of the good match between the model and the hardware, we could tune k_r, γ, and the cutoff frequency of the Butterworth filter offline, and no adjustments of the parameters were needed when we applied the method to the real hardware. The good quality of the learned step input does not introduce significant oscillations after the step. This and the large stability margins of the feedback loop allowed us to further increase the gain of the feedback controller for better amplifier noise and disturbance attenuation. The tuned parameters are given in Table VI. The gain of the feedback controller was increased by a factor of 1.5.

The reference profile for chopping is generated by applying the method described in [23]. This method generates a smooth fourth-order reference profile while taking into account the limits (maximum jerk etc.) of the plant.

In Fig. 12, the good match between the simulation and the experimental results is shown. After about 2.4 s (12 iterations), the repetitive controller has converged. The effect of activating the feedback controller after 4.7 s is clearly visible.

TABLE VI
TUNED PARAMETERS FOR REPETITIVE CONTROLLER FOR θ_x AND θ_y

DoF	k_r	γ	Cut off freq. [Hz]
θ_x	0.1	8	500
θ_y	0.5	9	500

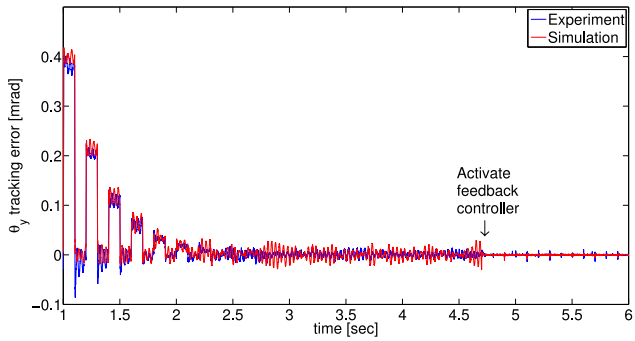

Fig. 12. Comparison of simulation result with experiment when tracking a 5-Hz chopping reference between 0 and 8.5 mrad in θ_y. Error convergence from 1 s onwards is shown. Feedback controller is activated after 4.7 s.

TABLE VII
MCCD REQUIREMENTS AND REALIZED PERFORMANCE

Description	Requirement	Result	Unit	Remark
Pos. stability	≤ 1.7	≤ 2.09	[μrad]	3σ
Pos. repeatability	≤ 1.7	≤ 0.4	[μrad]	
Pos. accuracy	≤ 85	≤ 1.04	[μrad]	
Settling time in θ_x	≤ 5	32	[ms]	applying
Settling time in θ_y	≤ 5	5.6	[ms]	rep. control
Parasitic z-disp.	≤ 200	≤ 3	[μm]	
Power dissipation	< 1	0.116	[W]	for 5-Hz chop
Peak currents	≤ 10	2.75	[A]	over 8.5 mrad
Thermal stability	≤ 1.7	< 1.7	[μrad]	

Positional stability is defined as $3\times$ rms (σ) level, all other requirements are defined as absolute maximum.

The compensator for θ_x is very similar, but here the resonances of the L-filter are matched with the 29.6- and 1440-Hz resonances of P_{θ_x}.

We use a practical approach for our repetitive controller design to be able to study its general performance without the need for S_p inversion of the high-order plant described in Table II. We are aware that small changes in the response can occur when applying a (zero phase) Q-filter and inversion of S_p. However, for θ_y, the tracking error is in the order of the reproducibility of the system, which means that for this DoF, no further improvements can be made. The performance of the repetitive controller and some considerations about the implementation of the method on the final MCC hardware are discussed in Section IV.

IV. EXPERIMENTAL RESULTS

All tests are performed with the test setup as described in Section II-A. Table VII summarizes the most important test results. All results, except for the settling time, are generated applying the hybrid controller. As we use the same feedback controller, most results are applicable to both control strategies. It is well known that the influence of stochastic disturbances (system noise and external vibrations) is amplified by the repetitive method [24]. Because of this, the positional stability is worse than for the hybrid approach. However, as discussed in Section III-B, we could compensate for this effect by increasing the loop gain of the feedback controller.

Most requirements are satisfied, but the positional stability specification and the settling time are not fully met. We believe that the positional stability can be further improved by fine tuning of the feedback controller in the final setup (when the exact noise and disturbance levels on the E-ELT platform are known), and by reduction of the amplifier range as discussed in Section III-A. In [25], the effectiveness of different strategies to reduce the negative influence of stochastic disturbances on positional stability when applying a repetitive controller is investigated. If required, this approach can be considered to further reduce the influence of stochastic disturbances on the positional stability of the plant.

The settling time results given in Table VII are generated by the repetitive controller. Fig. 13 shows the result of chopping in θ_y between 0 and 8.5 mrad for both the hybrid and repetitive methods. The hybrid controller converges within one chop cycle. The repetitive controller takes about nine cycles, but the settling time is much better. This is illustrated in Fig. 14, where a closeup of the settling behavior at the 8.5-mrad position after convergence is given. Since an observation typically takes minutes, the time required for learning (approximately 2 s) is easily compensated by the much better settling performance of the repetitive controller.

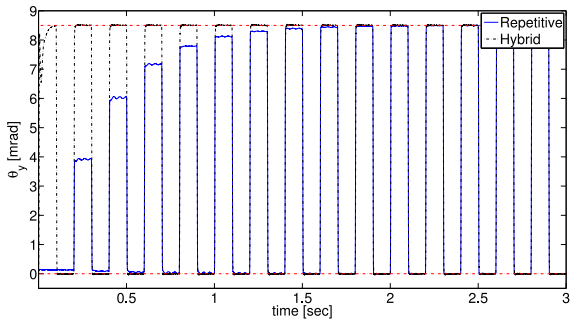

Fig. 13. Experimental result of 5Hz chopping in θ_y between 0 and 8.5 mrad, applying the hybrid and the repetitive controller.

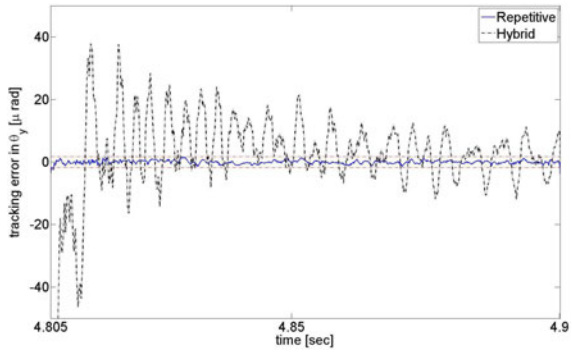

Fig. 14. Tracking error during 5-Hz chop after convergence (after 4.805 s at $\theta_y =$ 8.5 mrad position). Tracking of the hybrid controller is limited due to the nonlinearities which are not accounted for in the FF design.

As discussed in Section II-C, the quality of the FF signal applied in the hybrid method is limited as a result of the nonmodeled nonlinearities in the system. This limits the performance of any model based FF method. As argued in [9], the linear repetitive controller can deal with the small nonlinearity in the system and there is no need for adding extra complexity by applying a nonlinear repetitive controller.

The difference in the settling time for θ_x and θ_y can be explained by the resonant behavior of the experimental setup at approximately 500 Hz, which is only present in the θ_x-dynamics. Including the modeled resonance at 500 Hz in the L-filter design for θ_x did not improve performance because of the limited accuracy of the modeled resonance. More detailed modeling is required to correctly compensate for this effect in the L-filter design, but, as the resonance is part of the test setup and not of the MCCD hardware, we did not put further effort into solving this issue. Instead, the issue was taken up with the design engineers of the METIS team recommending to avoid low-frequency resonances in the structural interface of the MCC with the METIS instrument.

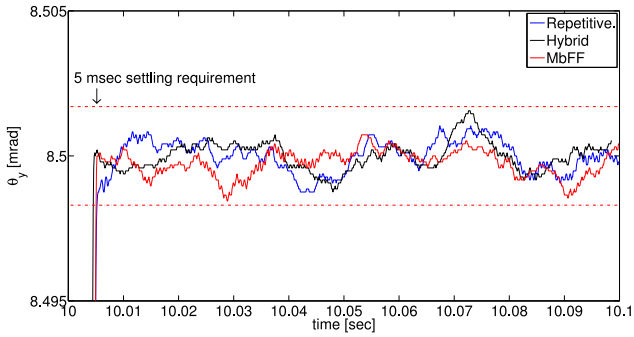

Fig. 15. Simulation of 5-Hz chopping between 0 and 8.5 mrad on the nonlinear plant, applying the repetitive, MbFF, and hybrid controller all using the FF-signal learned by the repetitive method. Closeup at 8.5-mrad position. Result after convergence of the repetitive controller and switching to closed loop. Red-dotted lines indicate 1.7-μrad positional stability limits.

When applying the repetitive controller, we ignored the typical design rule of monotonic error convergence ($|Q(1 - z^{\gamma} S_p k_r L)| < 1$), in order to maximize the learning bandwidth. Monotonic convergence is very important for the delicate hardware, but the necessary use of a Q-filter will limit the learning bandwidth of the repetitive controller. The realizable learning bandwidth strongly depends on the quality of the system identification and the ability of the L-filter to compensate for the resonances within the required learning bandwidth. If for the final hardware fast settling can only be achieved while ignoring the rule of monotonic convergence, the repetitive method will be used to generate a satisfactory FF signal, after which the learning is switched OFF. This FF signal can then be applied to either the MbFF or the hybrid approach. As discussed in Section III-A, which one to choose will depend on the final system configuration.

We tested this scenario in simulation on the nonlinear MCCD model by first applying the repetitive controller to the plant for a 0–8.5-mrad chop sequence. The repetitive method generates an FF signal which we then used as the FF input for both the MbFF and hybrid control strategies. A closeup of this simulation at the 8.5-mrad position after 10 s of chopping is given in Fig. 15. The different methods show comparable step results, which can be explained by the high accuracy of the FF signal (small positional errors during the step and accurate end position).

V. Conclusion

We tested the performance of the MCCD applying a new hybrid control strategy and compared the results to those when using a repetitive controller. The hybrid control strategy has been developed to eliminate the typical negative effect of the closed-loop controller on settling when tracking fast reference profiles applying the standard MbFF technique. Simulation results presented in Section III-A show that for the considered plant uncertainties, the hybrid method outperforms the MbFF technique when fast reference signals are applied.

Detailed system identification revealed the presence of non-negligible nonlinearities in the mechanism. The developed nonlinear plant model clearly explains the observed nonlinear behavior of the plant. Accurate tuning of the nonlinear system parameters is, however, difficult, and the approach was considered to be too complex for implementation in the final hardware. This limits the performance of any MbFF approach (including the proposed hybrid controller).

The results of the repetitive controller are very promising. We applied an open-loop learning approach to show the possible performance of the repetitive control strategy without the need for S_p inversion. The repetitive controller can handle the nonlinearities in the plant. When chopping in the θ_y-direction, we reach the reproducibility limit of the system, which means that we make maximum use of its capabilities.

As the repetitive method is a well-established control strategy with a firm mathematical background, and as it has shown its applicability to the hardware, this control strategy will be applied to the final MCC mechanism. If satisfying monotonic convergence limits the settling performance, the repetitive method will be used for learning of the FF signal offline, after which this FF can be applied to the MbFF or hybrid method.

The performed test program concludes the METIS Cold Chopper Demonstrator project. Because of the very promising results when applying the repetitive controller, it was decided not to change the MCC design significantly for the final hardware. This means no reduction of hysteresis in the actuators. We believe that detailed tuning of the feedback controller in the final setup and limiting the amplifier range will suffice to meet the positional stability requirement. Recommendations concerning the allowed resonance spectrum of the mechanical interface of the MCCD with the METIS instrument were provided to the METIS design team.

Acknowledgment

The authors would like to thank W. Horinga and B. Kramer for their support during the test campaign and J. Evers for valuable input on product and quality assurance. METIS is a collaboration between NOVA, UK-ATC, CEA Saclay, ETH Zürich, KU Leuven, MPIA, and A* Consortium (Austria). The MCCD project was funded by a generous ESFRI grant from NWO as part of the METIS development program. NOVA was responsible for the project management. The design and realization of the MCC hardware (mechanics and electronics) as well as the breadboard, qualification and lifetime testing were the responsibility of JPE BV. The NOVA—optical/infrared instrumentation group was responsible for the system engineering of the project. TNO provided general consultancy. The controller design and the performance test program of the mechanism was a combined effort of the University of Groningen and SRON.

References

[1] B. R. Brandl *et al.*, "METIS: the mid-infrared E-ELT imager and spectrograph," *Proc. SPIE*, vol. 9147, p. 914721, 2014, doi:10.1117/12.2056468.
[2] European Southern Observatory, "E-ELT instrument roadmap," The E-ELT construction proposal, ESO, C4: 3-32, 2012.
[3] A. Kovács, "Scanning strategies for imaging arrays," *Proc. SPIE*, vol. 7020, p. 5, 2008.
[4] M. Boerlage, M. Steinbuch, P. F. Lambrechts, and M. van de Wal, "Model based feedforward for motion systems," in *Proc. IEEE int. Conf. Control Appl.*, Istanbul, Turkey, 2003, pp. 1158–1163.

[5] D.E. Torfs, R. Vuerinckx, J. Swevers, and J. Schoukens, "Comparison of two feedforward design methods aiming at accurate trajectory tracking of the end point of a flexible robot arm," *IEEE Trans. Control Syst. Technol.*, vol. 6, no. 1, pp. 1–14, Jan. 1998.
[6] W. Singhose, "Command shaping for flexible systems: A review of the first 50 years," *Int. J. Prec. Eng. Manuf.*, vol. 10, no. 4, pp. 153–168, 2009.
[7] W. Singhose and J. Vaughan, "Reducing vibration by digital filtering and input shaping," *IEEE Trans. Control Syst. Technol.*, vol. 19, no. 6, pp. 1410–1420, Nov. 2011
[8] C. Li, D. Zhang, and X. Zhuang, "A survey of repetitive control," in *Proc. IEEE/RSJ Int. Conf. Intell. Robots Syst.*, Sendai, Japan, 2004, pp. 1160–1166.
[9] R. W. Longman, "Iterative learning control and repetitive control for engineering practice," *Int. J. Control*, vol. 73, no. 10, pp. 930–954, 2000.
[10] R. Huisman, J. Boomer, and B. Jayawardhana, "Hybrid control synthesis for output regulation with applications to fast motionnano-positioning mechanisms," to be published.
[11] R. Huisman and B. Jayawardhana, "On the design of hybrid output regulation for the METIS cold chopper," presented at the 7th IFAC Symp. Robust Control Design, Aalborg, Denmark, 2012.
[12] D. Roover and F. Sperling, "Point-to-point control of a high accuracy positioning mechanism," *Proc. Amer. Control Conf.*, Albuquerque, NM, USA, 1997, pp. 1350–1354.
[13] J. C. Clegg, "A nonlinear integrator for servomechanisms," *Trans. Am. Inst. Elect. Eng.*, vol. 77, (Part II): pp. 41–42, 1958.
[14] T. Tuma, A. Pantazi, J. Lygeros, and A. Sebastian, "Nanopositioning with impulsive state multiplication: A hybrid control approach," *IEEE Trans. Control Syst. Technol.*, vol. 21, no. 4, pp. 1352–1364, Jul. 2013.
[15] S. Paalvast *et al.*, "Development and characterization of a 2D precision cryogenic chopper for METIS," in *Proc. SPIE*, vol. 9151, p. 91510D, 2014.
[16] M. Eggens, "Results analysis METIS chopper mirror surface deformation," MCCD Project Documentation, DOC SRON-MCCD-RP-2011-00, 2011.
[17] D. C. Jiles and D. L. Atherton, "Theory of ferromagnetic hysteresis," *J. Magn. Magn. Mater.*, vol. 61, pp. 48–60, 1986.
[18] D. Lederer, H. Igarashi, A. Kost, and T. Honma, "On the parameter identification and application of the Jiles-Atherton hysteresis model for numerical modelling of measured characteristics," *IEEE Trans. Magn.*, vol. 35, no. 3, pp. 1211–1214, May 1999
[19] L. Marconi and A. R. Teel, "A note about hybrid linear regulation," in *Proc. 49th IEEE Conf. Decision Control*, Atlanta, GA, USA, 2010, pp. 1540–1545.
[20] R. Goebel, R. G. Sanfelice, and A. R. Teel, "Hybrid dynamical systems," *IEEE Control Syst. Mag.*, vol. 29, no. 2, pp. 28–93, Apr. 2009.
[21] M. Tomizuka, "Zero phase error tracking algorithm for digital control," *ASME J. Dyn. Syst., Meas. Control*, vol. 109, pp. 65–68, 1987.
[22] K. J. Åström, P. Hagander, and J. Sternby, "Zeros of sampled systems," *Automatica*, vol. 20, no. 1, pp. 31–38, 1984.
[23] P. F. Lambrechts, M. Boerlage, and M. Steinbuch, "Trajectory planning and feedforward design for high performance motion systems," *Proc. Amer. Control Conf.*, Boston, MA, USA, 2004, pp. 4637–4642.
[24] R. J. E. Merry, M. J. G. van de Molengraft, and M. Steinbuch, "Disturbances and model uncertainties in iterative learning control," in *Proc. 4th Int. Workshop Multidimensional Syst.*, 2005, pp. 136–141.
[25] M. Butcher, A. Karimi, and R. Longchamp, "A statistical analysis of certain iterative learning control algorithms," *Int. J. Control*, vol. 81, no. 1, pp. 156–166, 2008.

Robert Huisman received the B.S. degree in mechanical engineering from Hanze Hogeschool Groningen, Groningen, The Netherlands, in 1996, and the M.S. degree in astronomy and the Ph.D. degree in control theory and mechatronics from the University of Groningen, Groningen, in 2001 and 2016, respectively.

Since 2001, he has been with SRON—The Netherlands Institute for Space Research, Groningen, where he is currently an Instrument Scientist. His research interests include control of nanopositioning mechanisms and cryogenic mechatronics for space applications.

Sander Paalvast received the M.Sc. degree in mechanical engineering and the Ph.D. degree in mechanical engineering, both in the field of micromechatronic system design, from the Delft University of Technology, Delft, The Netherlands, in 2003 and 2010, respectively.

Since 2010, he has been with Janssen Precision Engineering B.V, Maastricht-Airport, The Netherlands. His research interests include the design, analysis, and control of mechatronic systems for accurate positioning and motion in ambient, (ultra) high vacuum, and cryogenic environments.

Bernhard R. Brandl received the B.Sc. and M.Sc. degrees in physics from Friedrich-Alexander Universitaet Erlangen-Nuernberg, Erlangen, Germany, in 1998 and 1991, respectively, and the Ph.D. degree in physics from Ludwig-Maximilians Universitaet, Munich, Germany, in 1996.

He was a Senior Research Associate at Cornell University, Ithaca, NY, USA, until 2003. He then moved to The Netherlands to join the faculty at Leiden Observatory, Leiden University, Leiden, The Netherlands. He currently holds a Chair of Infrared Astronomy with Leiden University and a part-time Chair of Astronomy and Instrumentation with Technical University Delft, Delft, The Netherlands. He is also the Principal Investigator of the Mid-Infrared European Extremely Large Telescope Imager and Spectrograph instrument for the European Extremely Large Telescope.

Teun van den Dool received the master's degree in engineering physics and control from the University of Groningen, Groningen, The Netherlands, in 1989.

At TNO, Delft, The Netherlands, he started as an Engineer in the development of acoustic monitoring and active noise and vibration control systems. Over the last 15 years, he has been working as a System Engineer developing optomechatronical systems mainly for semicon and space instruments for astronomy and earth observation, and for the oil and gas industries.

Martin Eggens received the B.Sc. degrees in mechanical engineering and electrical engineering from Hogeschool Drenthe, Emmen, The Netherlands, in 1995 and 1997, respectively.

Since then, he has been a Mechanical Design Engineer at SRON—The Netherlands Institute for Space Research, Groningen, The Netherlands. He is mainly involved in engineering of optomechanical design, analysis (vibration, thermal), alignment, and mechanisms of cryogenic space instrumentation and ground equipment.

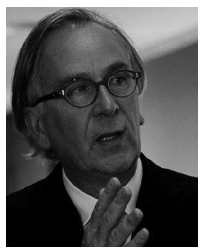

Huub Janssen received the Master of Science degree in mechanical engineering from the Eindhoven University of Technology, Eindhoven, The Netherlands, in 1985.

After several years of working at ASML, Veldhoven, The Netherlands, and Philips, Eindhoven, he founded Janssen Precision Engineering, Maastricht-Airport, The Netherlands, in 1991, a company excelling in precision engineering in ambient, vacuum, and cryogenic environments.

Gabby Aitink-Kroes received the B.Sc. degree in precision engineering from Hogeschool van Utrecht, Hilversum, The Netherlands, in 1995.

Since 1997, she has been an Optomechanical Instrument Engineer with NOVA(-ASTRON), Dwingeloo, The Netherlands, where she is involved in the design, development, and realization of (part of) cryogenic infrared instrumentation for professional ground-based (ESO VLT/VLTi), as well as space-based (ESA/NASA JWST) observatories. Her designs are to be recognized by the simplicity and the full use of 3-D space. She specializes in instrumental packaging and dedicated designs for cryogenic optics mounts and cryogenic mechanisms.

Frank Molster received the M.S. degree in astromineralogy and the Ph.D. degree in astronomy from the University of Amsterdam, Amsterdam, The Netherlands, in 1995 and 2000, respectively.

Afterwards, he was with Georgia Tech, Atlanta, GA, USA; ESA, Noordwijk, The Netherlands; HEspace, Noordwijk; NWO, The Hague, The Netherlands; Airbus DS, Leiden, The Netherlands; and NOVA, Leiden, Netherlands; and he is currently involved as a Manager for public private partnerships with the Leiden School of Instrumentmakers, Leiden. His research interests include scientific research instrumentation.

Maurice Teuwen received the M.S. degree in mechanical engineering from the Department of Precision Mechanics and Metrology, Eindhoven University of Technology, Eindhoven, The Netherlands, in 1999.

Since 1999, he has been with Janssen Precision Engineering, Maastricht-Airport, The Netherlands, initially as a Mechanical Lead Engineer and later as a System Engineer. In these roles, he has been involved in the development and realization of several optomechanical machines and instruments for applications in semiconductor industry, astronomy, physics research, and other related high-tech industries.

Mr. Teuwen has been a Member of the Editorial Board of the technical journal *Mikroniek* since 2015, which is published by the Dutch Society of Precision Engineering.

Lars Venema received the Ph.D. degree in physics from the University of Groningen, Groningen, The Netherlands, in 1994.

He conducted research at KVI, Groningen, and the RIVM National Institute of Public Health and Environmental Protection, Bilthoven, The Netherlands. Since 2002, he has been working with ASTRON, Dwingeloo, The Netherlands, on astronomical instrumentation, where he is currently a Senior Scientist in the field of optical astronomical instrumentation. He is the Systems Engineer for METIS, the Mid Infrared Instrument for the European Extremely Large Telescope.

Bayu Jayawardhana (SM'14) received the B.S. degree from the Institut Teknologi Bandung, Bandung, Indonesia, in 2000; the M.Eng. degree from Nanyang Technological University, Singapore, in 2003; and the Ph.D. degree from Imperial College London, London, U.K., in 2006, all in electrical and electronics engineering.

He is currently a University Reader with the Faculty of Mathematics and Natural Sciences, University of Groningen, Groningen, The Netherlands. His research interests include the analysis of nonlinear systems, systems with hysteresis, mechatronics, systems biology, and micronanotechnology.